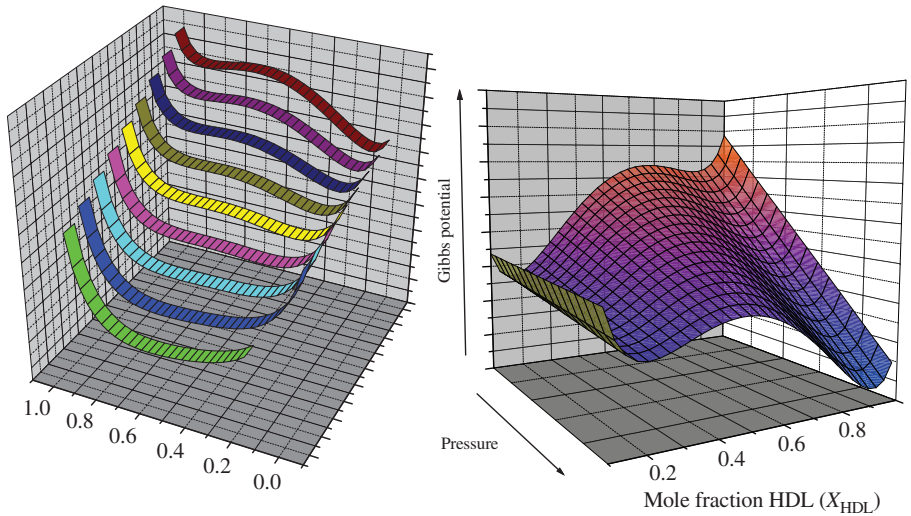

Figure 12.2. Free energy relations for liquids undergoing a first-order polyamorphic transition. Left: The evolution of the Gibbs potential (free energy of mixing, G_{mix}) as the temperature is reduced, for a two-state thermodynamic model that leads to a liquid–liquid phase transition at low temperature. The near axis is the relative proportion of low- versus high-density states present within the liquid. At high temperature, a single minimum is present in the free energy relation indicating that a single-phase homogeneous liquid is present, containing some proportion of high- and low-density domains or states in dynamic equilibrium. As the temperature is lowered, an instability appears recognized by a flattening in the G_{mix} versus T relation (marked LLPT in the diagram), followed by development of distinct minima appearing in the Gibbs potential at low versus high values of the mole fraction of the low- and high-density species. That behavior is indicative of a first-order phase transition occurring within the liquid, between high- and low-density polyamorphs at constant chemical composition. Right: The G_{mix} relations mapped as a function of pressure indicate changes in the relative stability of the low- versus high-density polyamorphic liquid phases.

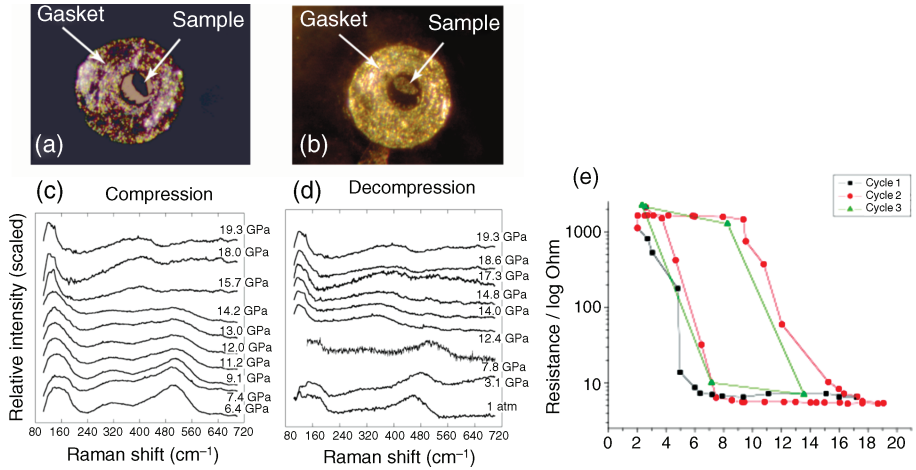

Figure 12.4. Evidence for pressure-induced polyamorphism in $a-$Si. Left panel: (**a**) and (**b**) Optical micrographs obtained for $a-$Si samples in the DAC taken below (a) and above (b) the LDA–HDA polyamorphic transition indicated by the Raman scattering data to occur near 14 GPa during compression. (**c**) Raman spectra for $a-$Si obtained during compression. The LDA–HDA transformation is clearly indicated by a rapid change in the spectra between 14–16 GPa. (**d**) Raman spectra obtained during decompression. The HDA polyamorphic form persists to lower pressure than on the upstroke, and LDA is first clearly observed below 8 GPa. Right: Electrical resistance measurements obtained for $a-$Si at high pressure in the DAC, obtained during three separate compression–decompression cycles. On the upstroke the sample remains semiconducting until above 11–12 GPa then rapidly becomes conducting between 12 and 16 GPa. During decompression, the conducting behavior persists to below 8 GPa and the initial semiconducting amorphous state is only recovered below approximately 4–6 GPa [103,104].

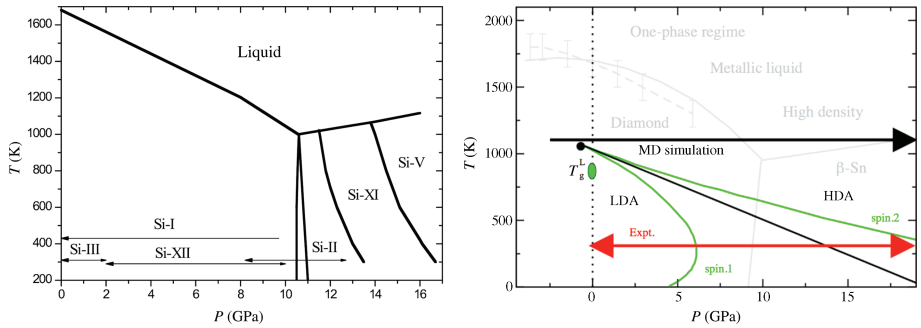

Figure 12.5. Left: P, T phase diagram of silicon in the range 0–17 GPa and 200–1700K. Solid lines indicate phase boundaries between the liquid and crystalline polymorphs. The diamond structured phase I is stable at low pressure. Si-II is isostructural with β-Sn. The high-pressure phases II, XI, and V are all metallic, as is the liquid. Phases III and XII are metastable [13]. Right: The two-state model applied to liquid Si, ignoring the presence of crystalline phases (shown in background). The critical point lies at slightly negative pressure: the LLPT line crosses the $P = 1$ atm boundary at 1060K. The glass transition for the low-density liquid form (T_g^L) is estimated to lie slightly below this, at 800–900K [104,105]. Spinodal boundaries for the low- and high-density polyamorphs are indicated by green line. The $T = 300$K experiments shown in Fig. 4 lie along the line of the red double arrow, and the MD simulations extended down to $T = 1100$K (black line and arrow).

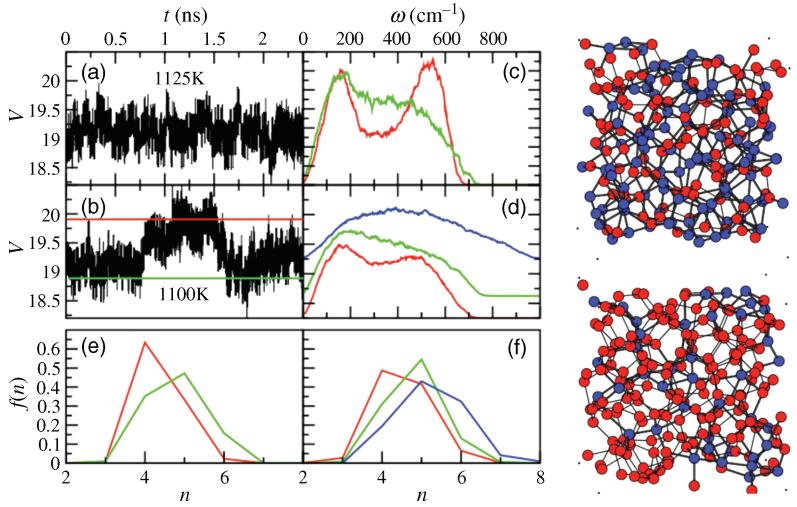

Figure 12.6. Results of constant pressure MD simulations of supercooled liquid Si using the Stillinger–Weber potential. Left panel: (**a**) As simulations were carried out at $P = 1$ atm down to $T = 1125$K, the equilibrated volumes exhibited normal thermal fluctuations over long simulation timescales (2.5 ns). (**b**) As the simulation temperature was reduced to 1100K, just above the expected HDL–LDL transition, we observed that the system experienced large and random volume excursions, indicating that it was sampling extrema of low- and high-density configurations. The average values of the upper (red) and lower (green) volume extrema corresponded to ~19.9 and ~18.8 Å^3, respectively, corresponding to a 5–6% difference between the two. We expect that these configurations evolve into the LDL/HDL liquid phases observed below the LLPT temperature. (**c**) Raman spectra calculated for the low (red) and high-density (green) subsets of simulated configurations at $T = 1100$K. (**d**) Simulated Raman spectra calculated for the supercooled liquid in the one-phase region at $T = 1125$K as P is increased (red-green-blue sequence of lines). The spectral changes are comparable with experimental observations (Fig. 4). (e) Coordination number ($\langle n \rangle$) changes and distribution corresponding to low- and high-density (green) states observed near the LLPT. The LDL states (red) have $\langle n \rangle = 4.38$, dominated by tetrahedral species but with a significant concentration of 5-coordinated sites; the HDL configurations (green) contain a larger proportion of 5-/6-coordinated sites. (f) Coordination number distributions calculated for the one-phase liquids well above the LLPT, at $T = 1125$K. At the lowest pressures (red) the system is predominantly 4-coordinated. As P increases (green, then blue), more 5- and 6-coordinated sites appear sequentially in the liquid structure. Right: Molecular graphics "snapshot" of a configuration of Si taken from a molecular dynamics simulation at 1075K and zero pressure, indicating the likely appearance of nanoscale low- and high-density domains within the single-liquid phase structure at temperatures just above the macroscopic T_c or T_{L-L} transitions that might be detected by future small-angle X-ray or neutron scattering studies. The atoms are colored by their nearest-neighbor coordination number (4-coordinate—red, 5-coordinate—blue). Regions high in 5-coordinate sites (HDL like) and in 4-coordinate sites (LDL like) are clearly evident.

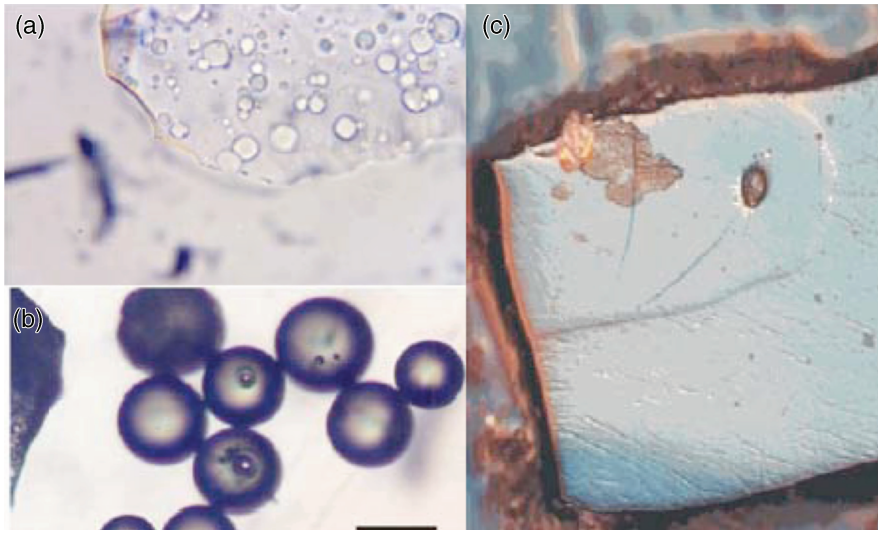

Figure 12.10. A density-, entropy-driven liquid–liquid phase transition was first encountered during quenching supercooled Y_2O_3–Al_2O_3 liquids [46,53,57]. Spherical inclusions of the LDL phase nucleated and grew within the HDL liquid, until arrested by the respective glass transitions, so that both were recovered as metastably coexisting glasses during rapid quenching experiments. (**a**) Photomicrograph of an AY23 glassy sample recovered from a roller quench experiment (field of view ∼200 μm). Subspherical LDA glassy inclusions that nucleated and grew during the quench are clearly visible within the HDA glassy matrix. The LDA and HDA polyamorphs are distinguished by their optical and mechanical properties, and from DTA/DSC calorimetry experiments [46–48,53,55]. (**b**) A close-up view of separated glassy LDA beads (the edge of a "matrix" HDA glass shard appears on the left of the picture). While most of the beads are solid and perfectly regular, some show circular voids or dimples indicative of cavitation related to a 4% volume change during the quench. (**c**) Larger samples could be formed by high-T melting in a Xe lamp thermal imaging furnace, and quenched by passing the molten droplets through a Pt wire grid [46–48,55,148,149]. Here, the polished sample shows coexisting LDA (top left) and HDA matrix regions. The glassy polyamorphs have different mechanical properties, resulting in a higher quality of polish for the LDA sample.

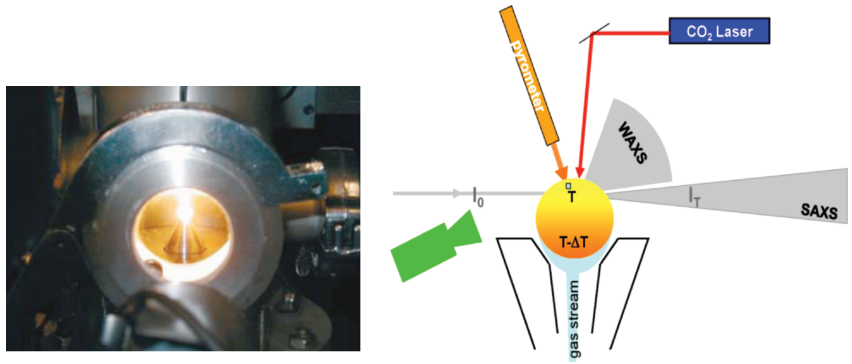

Figure 12.11. Left: A levitated ceramic liquid sample mounted inside an aerodynamic levitator at the APS for synchrotron X-ray scattering experiments. The conical levitator directing the air flow is seen at the bottom and the sample showing incandescent thermal emission is heated by a CO_2 laser. The levitator is mounted online at the synchrotron beamline, permitting X-ray small-angle and wide-angle scattering experiments. Right: Schematic of the aerodynamic furnace developed for SAXS/WAXS experiments. The laser and pyrometer are directed downward on to the drop that is supported by aerodynamic drag forces from a vertical stream of flowing Ar gas. The levitator is adjusted vertically for constant transmission (I_T/I_0) throughout the drop.

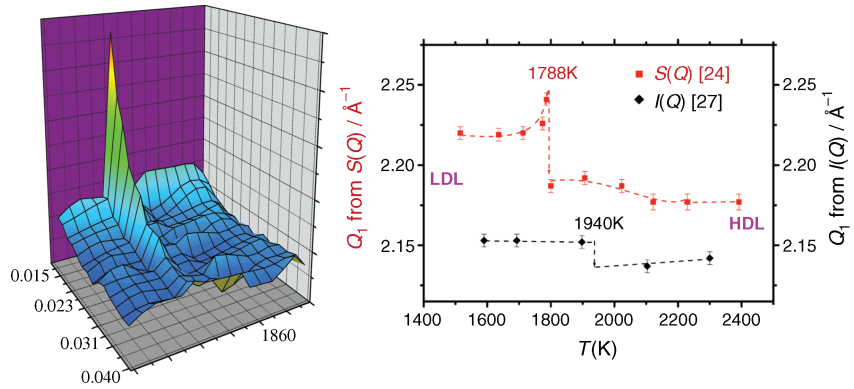

Figure 12.12. Left: Small-angle X-ray scattering data on levitated Y_2O_3–Al_2O_3 melts. These data were obtained during cooling into the deeply supercooled liquid regime [159,161]. The sharp rise in intensity at low Q values observed below 1800K is indicative of density fluctuations appearing in the liquid associated with the LLPT. Right: Note $S(Q)$ and $I(Q)$ removed temperature dependence of the position of the principal peak Q_1 in the structure factor $S(Q)$ (squares) [74,161] and in $I(Q)$ (diamonds) [148] observed in levitation studies [74] for two different compositions. Dashed curves highlight the discontinuity at 1788K due to the LLPT observed for AY20, and anticipated at 1940K for AY15 from the polyamorphic rotor temperatures [74] (Fig. 13).

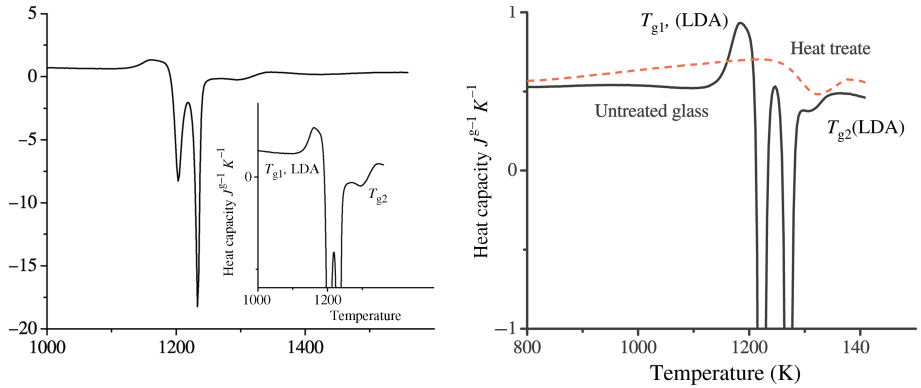

Figure 12.14. Left: Results of a differential scanning calorimetric study for a sample largely composed of HDA component of AY24 glass. The exotherm corresponding to the glass transition (T_g^{HDA}) is interrupted by an exotherm corresponding to some partial crystallization (a metastable Y_2O_3–Al_2O_3 garnet structured phase; ∼5% of the sample) followed by the exotherm corresponding to the LLPT into the LDA polyamorph. The glass transition for the LDA phase (T_g^{LDA}) occurs at higher temperature. Right: Successive DSC measurements for an AY24 sample, starting with the initial metastably quenched HDA phase (untreated glass). A second run was carried out with a second batch of the same sample that had been heated to above the LLPT at approximately 1280K. No evidence for the first glass transition (or the metastable recrystallization exotherm) was recorded, but only the T_g^{LDA} for the low-density polyamorph [46–48,54,55].

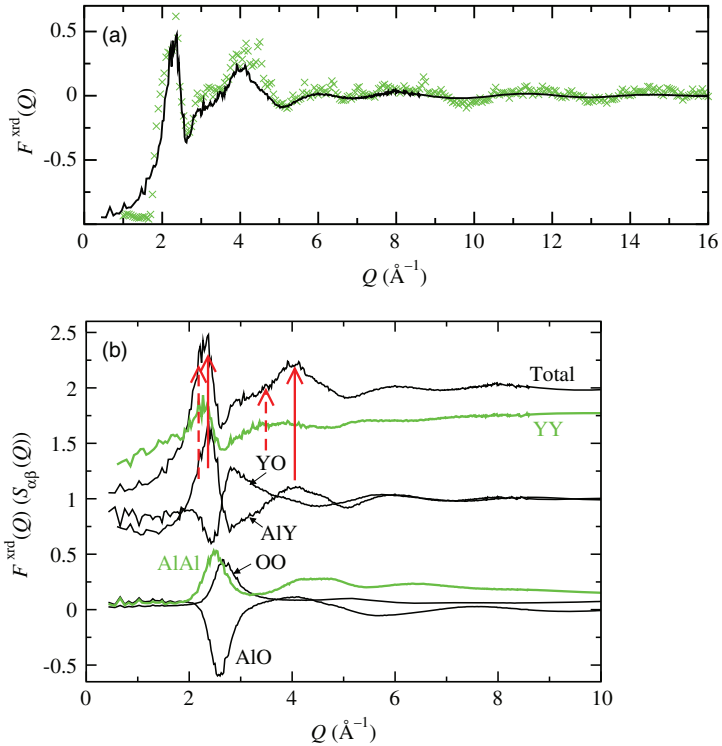

Figure 12.16. (**a**) Comparison of experimental (green crosses) and calculated (black line) X-ray total scattering functions for a polyamorphic AY20 glassy sample. High-energy synchrotron data (110 keV) were acquired at beam line 11-ID-C of the Advanced Photon Source (Argonne National Laboratory, USA). The many-body ion dynamics simulation results were generated from a run equilibrated at a constant temperature of 2400K over 2.2 ns of simulation timescale [150,151]. (**b**) Calculated X-ray partial structure factors between ion pairs for AY20 liquid simulated at 2400K [150,151]. The partial structure factors are shown weighted by the appropriate form factors and are shifted along the *y*-axis, for clarity. The upper (black) lines correspond to the total scattering function obtained by summing the individual partial structure factors in each case. The vertical arrows project the influence of the partial Al–Y (solid) and Y–Y (dashed) contributions to the first and second peak positions Q_1 and Q_2 of the measured $F(Q)$.

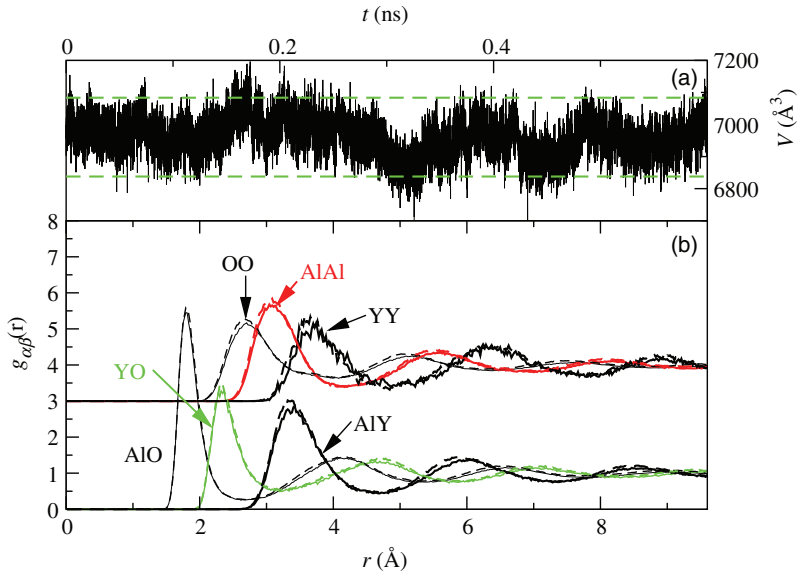

Figure 12.17. Upper panel: random volume fluctuations observed for an AY20 simulated liquid following equilibration at 2400K. Here, we show a typical fluctuation of the whole cell volume during a short (0.6 ns) section of the MD simulation at this temperature: such random volume fluctuations occurred during the entire simulation period [150,151]. The high- and low-density excursions that occur at two standard deviations away from the mean liquid volume are shown as light dashed lines. Lower panel: partial pair distribution functions calculated for the low- and high-density extrema using configurations colored by the cell volume limits shown above. The functions calculated from the high-density configurations are shown as dashed lines, and those from the low-density configurations as solid lines. The like–like functions (O–O, Al–Al and Y–Y partial rdfs) have been shifted relative to each other for clarity [150,151].

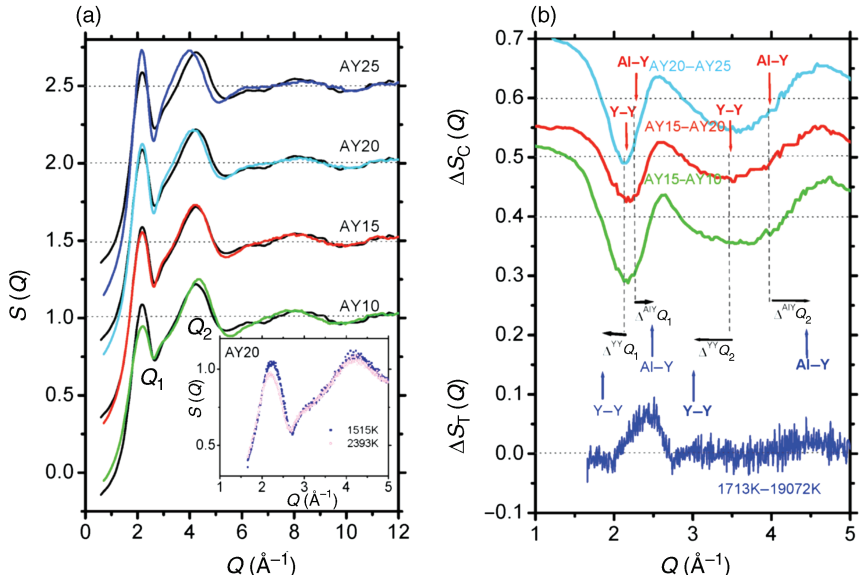

Figure 12.18. (**a**) Compositional dependence of the structure factor $S(Q)$ in AYx liquids measured using high energy 110 keV X-rays on station 11-1D-C at the APS. Data for different compositions are offset by 0.5 units along the y-axis for clarity. Each is compared to the $S(Q)$ reported previously in Ref. [161], represented by a black line. This data set identifies AY15 as the most likely composition studied in that work. Q_1 and Q_2 designate the principal and second peaks in $S(Q)$. The inset shows $S(Q)$ obtained from AY20 liquid at 1970K (filled black square) and 1713K (○) straddling the LLPT, measured using 16.9 keV X-rays on station 6.2 at the SRS. (**b**) Structure factor differences $[\Delta S_C(Q)]$ as a function of composition between different liquids (offset by 0.1 units for comparison), and in temperature $[\Delta S_T(Q)$ below] for liquid AY20. The Y–Y and Al–Y correlations are deduced from MD simulation studies. ΔQ_1^{YY} , ΔQ_2^{YY} and ΔQ_1^{AlY} , ΔQ_2^{AlY} are shifts with respect to features found in the experimental $\Delta S_T(Q)$ function [161].

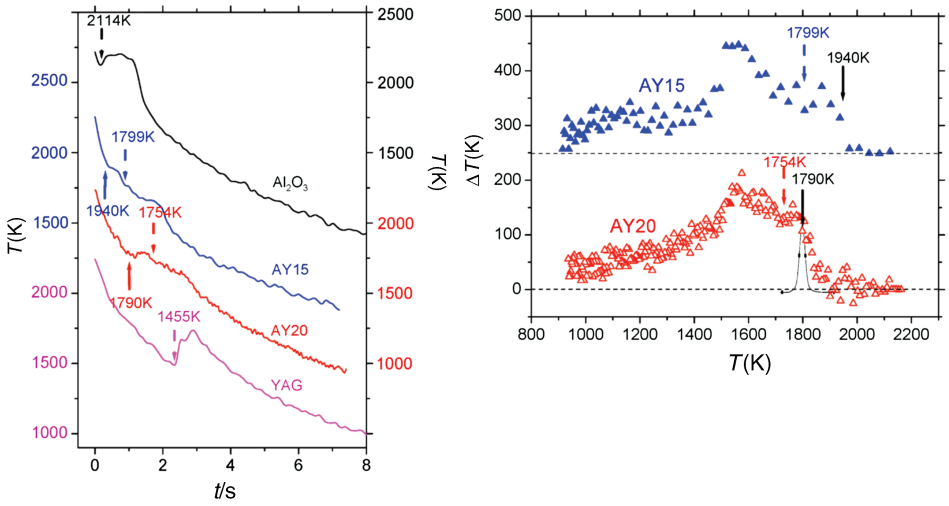

Figure 12.19. Left: Pyrometrically determined cooling curves for levitated AYx liquids showing crystallization temperatures where Debye–Scherrer features first appeared in the WAXS pattern (dashed arrows). For AY15 and AY20 the crystallization exotherm is anticipated by a prepeak (solid arrow) that is associated with the LLPT identified by the polyamorphic rotor action. Right: Curves for AY15 and AY20 with the cooling curves subtracted differentiating the LLTP exotherm from exotherm due to crystallization.

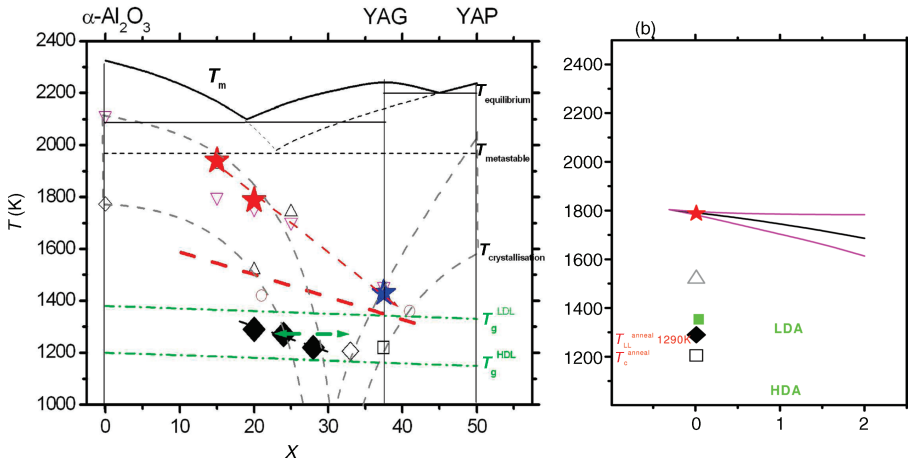

Figure 12.20. Left: Al_2O_3–Y_2O_3 (AYx) phase diagram extending from corundum ($x = 0$) to YAP ($x = 0.5$) superimposed on the equilibrium and metastable crystallization relations (see [57] for original data sources: also cited in text). LLPT temperatures determined *in situ* for levitated AY15 and AY20 are shown as light gray stars. The blue star for AY37.5 (YAG) is taken from cooling during levitation experiments [175]. The red line shows the compositional trend reported for liquids quenched with an Ir wire furnace and the green arrow the range for single phase glasses [57]. Filled diamonds are the LLTP temperatures obtained by annealing rapidly quenched HDA glass, between the glass transitions T_g^{LDL} and T_g^{HDL} indicated by green dash-dotted lines [46–48,54,55]. The remaining open points locate the observed crystallization temperatures (see Ref. [155] for original data sources), the dashed gray curves indicating the upper and lower limits. Right: T–P diagram for AY20 collating the LLPT measured *in situ* in the supercooled state [161] with the polyamorphic transition obtained by annealing rapidly quenched HDA glass [46–48,54,55]. The LLPT phase boundary with negative slope, $dT_{LL}/dP = \Delta V_{LL}/\Delta S_{LL}$, is plotted using experimental values of ΔV_{LL} and ΔS_{LL} [161]. The spinodal boundaries for the two-state model [7,26] converge on the liquid–liquid critical point that is located at slightly negative pressure [161], as is also the case for liquid Si (see Fig. 5).